Discrete scale invariance connects geodynamo timescales

A.R.T. Jonkers

Department of Earth and Ocean Sciences, University of Liverpool, 4 *Brownlow Street, Liverpool* L69 3*GP, United Kingdom. E-mail: jonkers@liv.ac.uk*

SUMMARY

The geodynamo exhibits a bewildering gamut of time-dependent fluctuations, on timescales from years to at least hundreds of millions of years. No framework yet exists that comprises all and relates each to all others in a quantitative sense. The technique of bootstrapped discrete scale invariance quantifies characteristic timescales of a process, based upon log-periodic fits of modulated power-law scaling of size-ranked event durations. Four independent geomagnetic data sets are analysed therewith, each spanning different timescales: the sequence of 332 known dipole reversal intervals (0–161 Ma); dipole intensity fluctuations (0–2 Ma); archeomagnetic secular variation (5000 B.C.–1950 A.D.); and historical secular variation (1590–1990 A.D.).

Six major characteristic timescales are empirically attested: circa 1.43 Ma, 56 Ka, and 763, 106, 21 and 3 yr. Moreover, all detected wavelengths and phases of the detected scaling signatures are highly similar, suggesting that a single process underlies all. This hypothesis is reinforced by extrapolating the log-periodic scaling signal of any particular data set to higher timescales than observed, through which predictions are obtained for characteristic scales attested elsewhere. Not only do many confirm one another, they also predict the typical duration of superchrons and geomagnetic jerks. A universal *scaling bridge* describes the complete range of geodynamo fluctuation timescales with a single power law.

Key words: archeomagnetism, core dynamics, geomagnetism, geomagnetic secular variation, palaeomagnetism, scale invariance.

1 INTRODUCTION

The Earth's internal magnetic field is most likely generated by dynamo action in the fluid outer core. Thermal and compositional buoyancy sources are thought to drive convection inside a rapidly rotating spherical shell of electrically conducting liquid, bounded by the mantle and the gradually growing solid inner core. In this environment reigns the non-linear interplay between buoyancy, Coriolis, pressure and Lorentz forces, causing mutual extreme sensitivity between fluid motions and magnetic field fluctuations (a tiny change in one may have a large effect in the other), across the widest range of scales known in geophysics (Glatzmaier *et al.* 1999; Roberts & Glatzmaier 2000; Zhang & Gubbins 2000; Dormy *et al.* 2000; Hollerbach 2003) The nature of this convective regime remains poorly understood, not least because analysis of time-dependent change has to contend with a broad diversity of observed fluctuations, from superchrons (extensive periods without reversals, timescale: 10^7 yr) through dipole chrons (intervals between successive reversals: 10^6–10^4 yr) and excursions (10^5–10^4 yr), the durations of reversals and excursions proper (10^3–10^4 yr), down to secular variation (10^4–10^{-1} yr) (Gradstein & Ogg 1996; Langereis *et al.* 1997; Hongre *et al.* 1998; Constable *et al.* 2000; Jackson *et al.* 2000; Hulot & Gallet 2003; Korte & Constable 2003; Valet *et al.* 2005). As each type of change represents a different facet of the same complex system, the questions whether and how their various

timescales are connected have immediate and far-reaching implications, for the theoretical domain and numerical and laboratory geodynamo simulation studies alike.

This study shows how the statistical detection of characteristic scales, in several geodynamo observables and over time, allows the construction of a universal *scaling bridge* that establishes a direct, quantified connection between palaeomagnetic superchrons, chrons, subchrons, dipole intensity fluctuations and (non-dipole) secular variation. It constitutes a coherent interpretation of internal geomagnetic fluctuations spanning over seven orders of magnitude in time as mere scale-dependent surface expressions of a single underlying process. In addition to several novel quantitative constraints on the physics, this approach furthermore yields predictions of other preferred geodynamo timescales outside the presently studied range of 10^0–10^7 yr. In the following, Section 2 outlines the method, Section 3 discusses the results of application to the four independent geomagnetic data sets, whereas the concluding Section 4 describes the scaling bridge.

2 METHOD

The detection of characteristic scales of a process requires analysis, first of general scale-invariant properties of the studied dynamics, and if present, to what extent this scale symmetry is adjusted. The

statistical fingerprint of scale invariance is a power-law probability distribution function: an observable's fluctuations (or durations of states) approximate a straight line on a log–log plot of, for example, rank versus size or magnitude of change versus associated duration or frequency. Power laws are ubiquitous in nature, quantifying, for example, size versus frequency of earthquakes, hurricanes and volcanic eruptions, as well as various scaling properties of natural fractals such as mountain ranges, coastlines, river networks, trees, clouds and blood vessels in mammals (West & Shlesinger 1989; Sornette 2004).

Regarding magnetic fields, power laws have previously been attested in the solar corona (flare event sizes, durations and energy release; Lu & Hamilton 1991; Lu *et al.* 1993), the geomagnetic reversal rate (Jonkers 2003) and in the power spectra of global geomagnetic intensity and intensity variations (Pelletier 1999, 2002; de Santis *et al.* 2003; Holme & Olsen 2006). Note that empirical power laws are always subject to cut-offs: at largest scales due to finite system size, available energy or observed time span and at smallest scales due to finite measurement resolution or physical limitations (e.g. the size of the fundamental constituent elements; Sornette 1998). Furthermore, the mere detection of 'featureless' scale-invariance in a process provides little constraint on the underlying physics. However, its provisional adoption as a working hypothesis is a prerequisite for disclosure of geophysically relevant information that *does* provide such information, through the concept of *discrete scale invariance*.

Discrete scale invariance (hereafter DSI), previously observed in, for example, earthquake precursors, material rupture, mammalian physiology and diffusion-limited aggregation, is the signature of *physical* structures of specific size and/or longevity that underlie a broad spectrum of observed changes (West & Shlesinger 1989; Sornette *et al.* 1996; Johansen & Sornette 1998; Sornette 1998; Johansen *et al.* 2000a). It is expressed in data as a series of log-periodic modulations superposed on a power law. Fig. 1(A) depicts a synthetic example, the triadic Cantor set. This simple fractal is generated from a single line segment by iterative removal of the middle third, leaving two smaller segments one-third in length. Consequently, for each increase in resolution by a factor three, the number of discernible parts doubles. This ratio is scale-invariant (as it remains constant regardless of absolute segment size), and is expressed by a power law. However, individual segments can be ranked and grouped by length, here plotted as horizontal levels, or *stratae*, in Fig. 1(A). These levels are called the fractal's *characteristic scales*, or *preferred scales*.

Characteristic scales are log-periodically spaced along the power-law slope, and can be said to break the symmetry of pure power-law scaling, that is, instead of featureless scale-invariance, the power-law probability distribution function is adjusted locally, since some absolute length scales are more likely (those forming a preferred scaling level), others less likely (the gaps between two adjacent levels), relative to the power-law expectation. Characteristic scales should not be confused with traditional statistical measures of central tendency such as mean, median or mode, nor with trends, or any kind of time-dependent periodicity. Given an observable of some non-linear system, DSI analysis instead examines its statistical ensemble of magnitudes (be it event sizes, durations or pairs thereof) for the presence of a log-periodic departure from pure power-law scaling.

Evidence of DSI indicates specific system-preferred fluctuation sizes and durations. These are often associated with some fundamental physical scale (either very large or very small) that provides the basis for cascade dynamics, producing a series of ever-larger or ever-

smaller preferred scales. These leave a distinct statistical signature that yields important (quantified) constraints on the underlying process, and that, moreover, cannot be detected by traditional methods such as Fourier spectral analysis, as the studied signal is statistically stationary rather than time-dependent. For an extensive introduction to DSI theory and many application examples in physics, see Sornette (1998). A detailed account of the method developed for the geomagnetic case ('bootstrapped DSI analysis') is given in a separate paper (Jonkers 2007); here only a brief outline is sketched.

Given an x-dependent observable O, $O(x)$ is scale-invariant under arbitrary magnification λx if a number $\mu(x)$ exists that satisfies:

$$O(x) = \mu O(\lambda x). \tag{1}$$

To illustrate this, recall the famous Gutenberg–Richter law in seismology. Rank all recorded shallow earthquakes by their seismic moment (so the largest moment is assigned rank 1, the second-largest rank 2 and so on), let $O(x)$ be their distribution, with x the rank and $O(x)$ the associated seismic moment. Scale-invariance is attested here if, regardless of a chosen initial size of moment, a change in that moment by a constant factor μ always yields a change in earthquake ranking by a constant factor λ. In this case, $O(x)$ is a power law with C a constant and exponent α:

$$O(x) = Cx^{\alpha}, \alpha = -\frac{\log \mu}{\log \lambda}. \tag{2}$$

When $O(x)$ is plotted as a straight line on a log–log scale, the constant power-law slope thus reflects the constant ratio of these two scale factors. The same applies when plotting the cumulative number of earthquakes that exceed a given moment against that moment.

Scale invariance is also a property of fractals, where it encodes geometrical self-similarity of a set divisible into subsets that resemble the whole over a range of scales. However, many fractals obey scale invariance only for specific choices of magnification (or resolution). This *discrete* scale invariance is a weaker form of power-law scaling, describing parts self-similar to the whole *only* at resolutions equal to some multiple of a characteristic scale. Given a mathematical, noise-free fractal, if magnification increases continuously, the number of discernable parts will increase at these specific resolutions only, while remaining constant over the interval between any two neighbouring characteristic scales. The scaling relationship thereby becomes modulated:

$$O(x) = Cx^{\alpha} P\left(\frac{\log x}{\log \lambda}\right), \tag{3}$$

with P a function of period unity. Both power law and superposed modulation are essential constituents of this definition; the latter cannot exist on its own, as it is defined by its departure from the former. Although log-periodicity could in theory be imposed on other types of probability distributions as well, the resulting statistics would no longer be scale-invariant, leaving the physical interpretation of the generating process ambiguous or meaningless. Moreover, this notion does not apply to the geodynamo analyses presented here, where power laws abound (see below); therefore, they fall outside the scope of this paper.

By expanding P in eq. (3) into a Fourier series:

$$P\left(\frac{\log x}{\log \lambda}\right) = \sum_{n=-\infty}^{\infty} a_n \exp[i 2\pi n(\log x / \log \lambda)] \tag{4}$$

$O(x)$ can be described as a sum of power laws with n an arbitrary integer and a (theoretically infinite) set of complex exponents:

$$O(x) = Cx^{\alpha}, \alpha = -\frac{\log \mu}{\log \lambda} + i\left(\frac{2\pi n}{\log \lambda}\right), \tag{5}$$
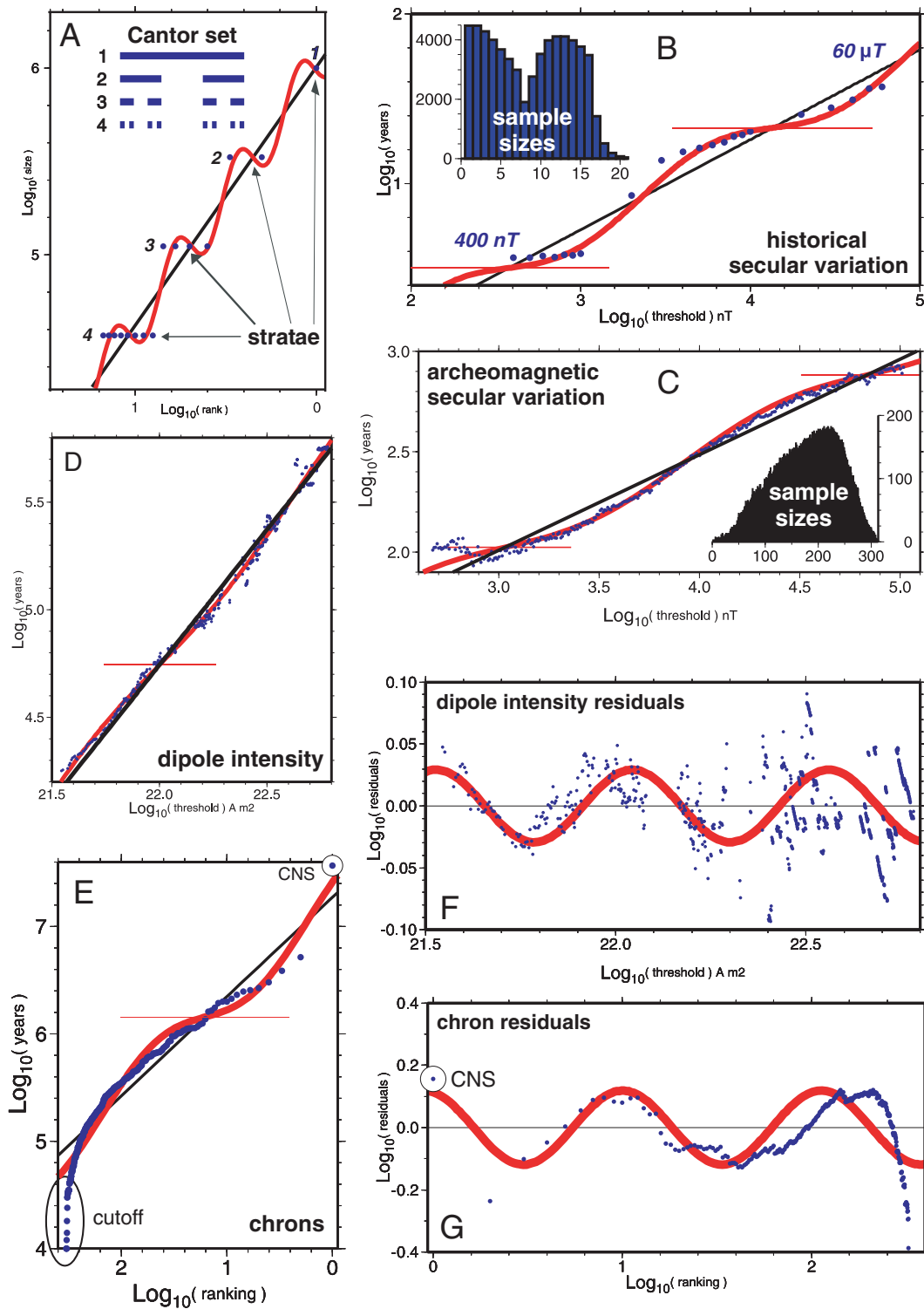
Figure 1. Temporal discrete scale invariance (DSI) consists of a power law (black line) and superposed modulation (red line, horizontal bars mark preferred timescales, see Table 1). (A) Ranked segment sizes of the Cantor set; (arbitrary) initial length: 10^6 units, first four resolutions shown (*x*-axis reversed). (B) Average time before an absolute threshold of change (400 nT–60 μT, $N = 21$) is exceeded in historical secular variation at the core–mantle boundary; inset histogram depicts sample size per metadata point ($N = 61\,166$; larger thresholds toward right). (C) Average time before a threshold (380–139 601 nT, $N = 313$, based upon 30 557 significant results, in histogram per point) is exceeded in archeomagnetic secular variation at the core–mantle boundary. (D) Time before virtual axial dipole moment exceeds a given threshold ($N = 793$, ranging from 0.35 to 6.6×10^{22} $A\,m^2$). (E) Ranked chrons (Mesozoic to present, Cretaceous Normal Superchron (CNS) included; $N = 332$). The diffusion timescale of the inner core ($\sim$10 Ka) imposes a physical cut-off to power-law scaling at bottom (*x*-axis reversed). (F) Residuals of the DSI signal in panel D; data become progressively more noisy for larger thresholds. (G) Chron DSI residuals (CNS included).

through which continuous scale invariance is recovered for the special case $n = 0$, that is, eq. (5) is a more general expression of (2). The complex solution of $n \neq 0$ implies a characteristic scaling factor λ, expressed as a log-periodic correction to pure power-law scaling.

Returning to the generic example of the Cantor set (after Sornette 1998), Fig. 1(A, top left) depicts the first few iterations of its formation. Given this spectrum of line segments, each one provides one length datum to a data set, which, when sufficiently large for analysis, is rank-ordered by size. Thus the original, single segment length is given rank 1, the next two (both one-third the original size) are assigned rank 2 and 3, respectively, the next four (one-ninth the original size) span ranks 4–7, and so forth. No binning is performed, as it could degrade the signal of interest. Plotted on a log–log scale of rank versus segment length, the resulting power-law slope α is, at first approximation:

$$\alpha = -\frac{\log 2}{\log 3}. \tag{6}$$

However, the actual point distribution of sizes consists of a number of distinct stratae along the power-law slope, separated by scale 'gaps'. Following eq. (5), the power-law exponent can be restated more generally as:

$$\alpha = -\frac{\log 2}{\log 3} + i\frac{2\pi n}{\log 3} \tag{7}$$

with the imaginary part directly controlled by the preferred scaling ratio three under which the set is exactly self-similar. Note that line segments map onto differently sized segments not only at magnifications of three, but also at any negative or positive integer power thereof.

The Cantor set is, however, artificial, in consisting of stratae only. By contrast, natural phenomena, being affected by noise and external processes, exhibit intermediate sizes (or durations) everywhere along the observed modulation (see Jonkers 2007, fig. 5, for an example of Cantor synthetics with added noise). The identification of characteristic scales in empirical data thus entails finding a statistically significant, coherent adjustment to power-law scaling *everywhere* along its slope, making the likelihood of some sizes (durations) slightly larger, others smaller, than predicted by the power law alone. DSI analysis is emphatically not dependent on the interpretation of local scaling features resembling a strata, but rather, on the entire spectrum of fluctuations captured. Preferred length scales are consequently identified through the wavefunction that best fits *all* points, a more robust approach. Let the observed *x*-range be specified by:

$$\begin{aligned} X_0 &= \min[\log_{10}(x)] \\ X_{\text{range}} &= \max[\log_{10}(x)] - X_0. \end{aligned} \tag{8}$$

Within the log–log domain, given power-law intercept C and slope α, and modulation frequency f, phase ϕ and amplitude β, the DSI equation to be fitted is:

$$Y = C + \alpha x + \beta \cos\left\{\varphi + f2\pi\left[\frac{\log_{10}(x) - X_0}{X_{\text{range}}}\right]\right\} \tag{9}$$

with any residual scaling signal of higher harmonics (*2f*, *3f*, . . .), if at all detectable, expressed with much smaller residual amplitude (to be discussed below). Eq. (9) allows the $\log_{10}(x)$ coordinate of the two nodes (X_{n1} and X_{n2}) within one wavelength to be determined through:

$$\begin{aligned} X_{n1} &= X_0 + (0.25 - f\varphi)(X_{\text{range}}/f) \\ X_{n2} &= X_0 + (0.75 - f\varphi)(X_{\text{range}}/f) \end{aligned} \tag{10}$$

which, when inserted in eq. (9) yield the other scaling coordinate per node (i.e. Y_{n1} and Y_{n2}). The fitted phase ϕ thus codes the nodal distance relative to X_0, the lower bound of the observed range. Other nodes may be found by adding integer values to the numeric term (0.25 c.q. 0.75) in eq. (10). Note that only one of these two nodes represents a strata; the other one coincides with the near-vertical intersection of modulation and power law, the least-preferred scales. Proper identification is dependent upon the signs of the power-law slope and of the amplitude (both non-zero by definition). Given a positive amplitude, the stratae are associated with X_{n1} for a positive slope, and with X_{n2} for a negative slope; alternatively, given a negative amplitude, the reverse is true. Lastly, if multiple stratae are captured in data, the largest preferred scale is the strata closest to X_0 for a negative slope, but closest to $X_0 + X_{\text{range}}$ for a positive slope.

A geomagnetically relevant example of this scaling lacunarity is the breakup of large eddies in weakly turbulent flow into only a few smaller ones, which themselves break up following the same approximate ratio, all translations being a multiple of a fundamental discrete generator, making some gyre sizes more likely to occur than others (Novikov 1990; Johansen *et al.* 2000b; Zhou & Sornette 2002). Whereas the derived power-law slope represents the ratio with which the number of discernible gyres (or processes) increases with observational resolution, DSI yields their characteristic length scales and longevity. As stressed earlier, no temporal periodicity (e.g. a Fourier spectrum peak) is implied, but merely that, due to underlying physical constraints (notably, threshold dynamics), some particular fluctuation sizes and associated durations are more (c.q. less) likely to occur, in a probabilistic sense, than would be expected under the assumption of a power-law probability distribution.

As the hallmark of DSI is a log-periodic modulation superposed on a power law, possibly including higher-order harmonics of much reduced amplitude, the detection of DSI requires statistical testing and parameter quantification of: (1) the power-law baseline and (2) any significant, coherent residual modulation(s) spanning at least one wavelength. In the current context, for each data set numbering more than ten size-ranked durations, power laws were fitted with weighted least squares, which assumes that the remaining errors approximate a Gaussian distribution. If a different distribution were strongly suspected, one may adjust either the fitting procedure, the weighting, or both. Confidence limits associated with these fits were determined with Kuiper's statistic, related to the two-tailed non-parametric Kolmogorov–Smirnov (K–S) test of goodness-of-fit. Whereas the K–S test is most sensitive around the median, Kuiper's statistic is equally sensitive at all points, and was applied at an α-level of 10 per cent (i.e. the 90 per cent statistical confidence limit). This relatively moderate threshold was used because DSI implies that no pure power law will be found. The frequency f of the modulation was determined using Lomb periodograms of the power-law residuals, using oversampling factor 10. This type of spectral analysis was chosen over Fourier analysis because it exploits the uneven point density of logarithmic spacing, and additionally quantifies the type II-error (the probability of unwarranted acceptance, a.k.a. false attribution probability) associated with the frequency of maximum power.

Matrix inversion with L_2-norm (again assuming approximately Gaussian-distributed errors) yielded best-fitting estimates of phase φ and amplitude β, as well as rms errors of the amplitude residuals. Determining f and φ allows quantification of actual preferred scales of the studied process, with f quantifying the log-periodicity (the size of the gaps between preferred scales) and φ a time normalization in the log–log domain used to identify the coordinates of individual levels. DSI amplitude β can be interpreted as a measure of the

intensity of symmetry breaking (i.e. the departure of observed scales from a pure power law). Variance and standard deviation of the frequency fit itself were obtained through bootstrap Monte Carlo simulations ($N = 1000$ per observable, per data set), and multiplied by an appropriate distance factor to obtain error margins beyond the observed time range (see next section). Finally, scaling stratae were obtained using eqs (9) and (10). It is these scaling 'plateaus' that are of most interest, because across the range of points forming a strata the associated durations remain almost constant, whereas under a pure power-law assumption they would be expected to follow the power-law slope.

The most straightforward application of DSI analysis is to a ranked data set (here, dipole reversal intervals). Time-series analysis, however, most often relies on one or multiple sequences of an observable's values sampled equidistantly over time. Both dipole intensity fluctuation data and secular variation time-series fall into this second category. *Bootstrapped DSI,* developed by the author, is a two-stage DSI analysis (not to be confused with bootstrap Monte Carlo simulations) to deal with this more common type of data. A comprehensive treatment of its general application is given in a separate publication (Jonkers 2007). Briefly summarized in three steps:

1. A large number of thresholds of absolute change x_i are defined within data range; for each threshold, a subset is compiled of time intervals τ_i from a reference point to a later point that exceeds the current threshold, with each endpoint becoming the new reference for the next duration.

2. Each duration subset with more than ten members is ranked and subjected to DSI analysis; those with statistically significant DSI yield one meta-datapoint each, consisting of the largest preferred timescale T_i and the threshold x_i that generated that subset.

3. DSI analysis of the metadata (x_i versus T_i), if significant, yields one or more preferred timescales, associated with a preferred fluctuation scale expressed in the original observable.

Regarding step 1, single-time step threshold crossings are to be excluded, causing the number of intervals larger than unity (per subset) at first to increase sharply with increasing threshold (the peak in signal strength), before gradually decreasing to zero again (at some point a threshold is reached that is never crossed within the time-series). One might expect the number of intervals simply to decrease monotonically with increasing threshold, as small changes occur more frequently than large ones. However, the sharp initial rise is due to the growing number of durations exceeding a single time step. Tiny thresholds will consist exclusively of single-time step threshold crossings, which are excluded, generating empty sets. With larger thresholds, the ratio of single (invalid) versus multiple time step durations (valid) will increasingly favour the latter, causing the initial rise. Once all intervals consist of multiple time steps, the gradual fall-off will start for larger thresholds (see fig. 3 in Jonkers 2007). To reduce noise, the few values preceding this early peak in signal strength are discarded, as they (1) are most prone to observational error and (2) do not sample the complete spectrum of fluctuations, producing spurious results. Those remaining subsets that contain both a statistically significant power law and a significant DSI signature each yield a largest preferred timescale T_i (the highest recorded strata per subset). This duration is reunited with the threshold that initially produced it, in a meta-data set of x_i versus T_i.

The metadata are subjected to DSI analysis in the last stage of the bootstrap process, applying the same statistical criteria of acceptance as before. Assuming that a statistically significant power law and

modulation are again attested, the resulting scaling stratae in the metadata identify one or more preferred timescales, each associated with a distinct range of thresholds. Unlike the initial analyses (which used rank as x-coordinate), the metadata thus associate a preferred timescale directly with a specific range of the original observable. In addition, the bootstrap process acts as a low-pass noise filter, by exploring the coherence of a large range of thresholds, rather than interpreting a single ranked set of intervals.

More importantly, if the investigated scaling phenomenon is log-periodic, it is possible to extend the modulation along the power-law slope beyond the observed range in both directions (i.e. to shorter and longer timescales than observed) to obtain predicted preferred scales, for direct comparison with those of other data sets generated by the same complex system. Thereby, a normalization in terms of timescales is achieved, that is, applying the bootstrapped DSI method to a number of different observables deemed to originate from the same source, their potential coherence in the temporal domain can be quantified, and possibly even unified. The investigated observables need not be the same; indeed, from a standpoint of independent confirmation it is preferable that they are not, sharing only the same temporal axis, but not necessarily overlapping in temporal range. The geodynamo provides a case in point.

3 GEODYNAMO RESULTS

Four geomagnetic data sets were subjected to extensive DSI analysis:

(1) The sequence of known reversal intervals (chrons and subchrons) from 161 Ma to the present day (Gradstein & Ogg 1996).

(2) Global dipole intensity fluctuations over the last 2 Ma (*SINT2000* data set; Valet *et al.* 2005).

(3) Local dipole-detrended archeomagnetic secular variation at the core–mantle boundary (field map *CALS7K.2*, 5000 B.C.–1950 A.D.; Korte & Constable 2005; Korte *et al.* 2005).

(4) local dipole-detrended historical secular variation at the core–mantle boundary (field map *gufm1*, 1590–1990; Jackson *et al.* 2000).

Not only do these four data sets stem from completely independent sources (lava flows, ocean floor sediments, lake floor sediments and archeological artefacts, and historical observations, respectively), they measure different geodynamo phenomena, with different temporal resolution (10^4, 10^3, 5 and 1 yr are used here, respectively), and their time spans overlap marginally at best. In other words, only communal, scale-invariant features would be able to bridge these gaps.

Data processing proceeded as follows. For ranked chron data (intervals between successive reversals), DSI analysis was performed twice: once with, and once without the Cretaceous Normal Superchron (CNS). In the case of time-series (the three other data sets), the more elaborate bootstrap DSI method was deployed, yielding more accurate results. The *SINT2000* data set constitutes a single time-series of dipole moment (in A m^2). To analyse the time-dependent global field map *gufm1*, time-series of the non-dipole field per orthogonal vector component (X, Y, Z, i.e. the eastward, northward and radial part of the field, in nT) were extracted for each cell in a $6° × 6°$ grid (i.e. $30 × 60 × 3 = 5400$ time-series, sampled annually, $N = 401$). A similar procedure was applied to field map *CALS7K.2*, but due to its lower spherical harmonic resolution, using a grid resolution of $30° × 30°$, yielding $6 × 12 × 3 = 216$ time-series (sampled every 5 yr, $N = 1391$). Note that if regular grids are employed on a non-Euclidean surface (such as a sphere), area-dependent weighting is to be applied to local results to obtain globally averaged meta

Table 1. Observed preferred geodynamo scales, in intensity and time.

Data set	Spherical harmonics	Characteristic fluctuation	Associated duration	DSI strata in $\log_{10}(\text{yr}) \pm 2\sigma$
Historical SV	2—14	378 nT	3.18 yr	0.503 ± 0.05
		13 532 nT	21.29 yr	1.328 ± 0.05
Archeomagnetic SV	2—10	1072 nT	105.56 yr	2.024 ± 0.02
		68 469 nT	762.58 yr	2.882 ± 0.02
Dipole intensity	1	1.0037×10^{22} A m^2	55.58 Ka	4.745 ± 0.04
Chrons (+CNS)	1	unknown	1.43 Ma	6.156 ± 0.16

Note: SV, secular variation; DSI, discrete scale invariance; CNS, Cretaceous Normal Superchron.

datapoints per threshold. Conversely, no such weighting is to be used when an equal-area grid is employed instead.

An alternative, computationally more efficient approach subjected the spherical harmonic Gauss coefficients of these two field maps directly to DSI analysis. Out of the 224 Gauss coefficients that describe *gufm1* at any particular time, 72 exhibited a statistically significant scaling signal, whereas for *CALS7K.2*, a total of 77 out of 120 fell into this category. A mere 21 Gauss coefficients tested positive in both: $g_2{}^1, g_3{}^0, g_3{}^1, h_4{}^2, g_5{}^0, h_5{}^4, g_6{}^1, h_6{}^2 h_6{}^3, h_7{}^2, g_7{}^5, h_7{}^7, g_8{}^2, h_8{}^2 g_8{}^7, h_8{}^7, h_9{}^6, g_{10}{}^3, g_{10}{}^4, g_{10}{}^7$ and $g_{10}{}^8$. In both cases, the spatial decomposition of preferred scales yielded ranges of scales consistent with the results obtained from local field vectors. There are, however, several reasons why the latter are considered here, in terms of global averages per threshold, rather than using the findings from the Gauss coefficients. First, many archeomagnetic Gauss coefficients, in particular the higher degrees, suffer from considerable amounts of noise when studied individually, whereas the overall DSI profile based upon local vectors is far more robust. Secondly, the present aim is to compare scale-invariant traits of the geodynamo as a single system, examining dipole and non-dipole parts as global entities. Thirdly, the decomposition into Gauss coefficients causes wide disparities in their individual threshold ranges, complicating the process of attaining a single global scaling profile. Lastly, spatially heterogeneous DSI profiles, both in terms of local field components and breakdown into specific Gauss coefficients, are the subject of ongoing separate investigations that incorporate empirical data and a range of numerical geodynamo simulations. Their intricate nature falls outside the scope of this initial study, warranting a separate, future publication.

In addition to primary data analysis, the possible presence of a *residual* DSI modulation has also been investigated. Regrettably, due to limited computing capacity, it proved prohibitively expensive to enable a statistically significant residual modulation to be determined for secular variation (a task to be addressed in future work). However, the palaeomagnetic data sets of dipole intensity and chrons did allow meaningful analysis of residuals. Thereto the appropriate value of the first-found power-law modulation was subtracted for each point, followed by a new periodogram and phase and amplitude fit of the residuals, followed by significance tests and determination of predicted preferred timescales (stratae), as before. Formally, in analogue to eq. (9), data residuals γ_{res} were computed by subtracting the best-fitting DSI modulation from the observations γ_x:

$$\gamma_{\text{res}_x} = \gamma_x - C + \alpha x + \beta \cos\left\{\varphi + f 2\pi \left[\frac{\log_{10}(x) - X_0}{X_{\text{range}}}\right]\right\} \tag{11}$$

followed by a second wave fit Y_{res} of these residuals, this time naturally without a power-law component:

$$Y_{\text{res}} = \beta_{\text{res}} \cos\left\{\varphi_{\text{res}} + f_{\text{res}} 2\pi \left[\frac{\log_{10}(x) - X_0}{X_{\text{range}}}\right]\right\} \tag{12}$$

Note that these fits of residuals were performed independently of prior DSI parameters found for the original observables (other than generating the residuals in the first place), that is, neither the residual frequency, nor the phase, nor the amplitude were constrained a priori to conform, or otherwise relate, to the values found for primary data. To determine a confidence level associated with the new frequency estimates, an identical strategy as before was followed, running 1000 bootstrap Monte Carlo simulations for each set, quantifying the variance of the periodogram peak.

In theory, a significant residual frequency f_{res} could be an entirely different DSI signal, indicating two interfering dynamics that produce their own distinct log-periodic series of preferred scales. However, the very nature of DSI predicts that higher harmonics of the same fundamental frequency are to be expected if data accuracy permits. Applying Occam's razor, one should always evaluate first to what extent f_{res} in eq. (12) can reasonably be interpreted as *2f* in (9), the next likely frequency given the expansion in (5). Naturally, residuals are plagued to a much larger relative degree by noise and error than primary data are; perfect agreement in all DSI parameters is expected only of synthetic fractals. So even though the assumption of $f_{\text{res}} = 2f$ yields the expectation of an approximately doubled number of stratae for any sufficiently large scale interval, communal stratae will not necessarily coincide exactly. See Johansen & Sornette (1998) for similar cases as observed in diffusion-limited aggregation and a model of rupture.

As is evident in Fig. 1, all primary data sets exhibit a DSI modulation, with the palaeomagnetic data sets additionally allowing the first residual frequency f_{res} to be determined. Six main preferred timescales of the geodynamo are thereby observed, listed in Table 1. They support the existence of short-term secular variation (2–5 yr), intermediate-term secular variation of $O(10 \text{ yr})$, long-term secular variation of $O(100 \text{ yr})$, and preferred dipole fluctuations on timescales of $O(10 \text{ Ka})$ and $O(1 \text{ Ma})$, respectively. However, how reliable are these estimates, and does this constitute proof of the existence of characteristic scales?

Each individual point plotted in Fig. 1, panels B–G, represents a meta-coordinate $T_i(x_i)$ as described in the previous section, resulting from a DSI subset analysis that satisfied the following conditions: number of points greater than 10, non-zero negative power-law slope, Lomb periodogram type-II error below 0.1, non-zero amplitude, rms residuals of the DSI fit are smaller than those from the power-law fit alone, both power-law fit and DSI fit satisfy the Kuiper test at a two-sided confidence level of 10 per cent, and quantified stratae are within observable range. The resulting statistics are as follows. The dipole chrons, a single data set of durations (spanning 10 Ka–36 Ma, *ca.* 3.5 orders of magnitude) yielded two significant DSI results: with, and without the inclusion of the CNS. In *SINT2000*, a total of 1250 thresholds (spanning 0.35–6.60×10^{22} A m^2, *ca.* 1.8 orders of magnitude) yielded 1142 subsets (91.4 per cent of the total) with statistically significant DSI (of which 793 mapped the highest recorded scaling strata; the remaining ones

captured the next lower one). For field map *CALS7K.2*, 313 thresholds were imposed (spanning 380–139 601 nT, *ca.* 2.6 orders of magnitude); 67 608 analyses were performed, of which 43 765 (64.7 per cent) yielded statistically significant DSI results (of which 30 557 mapped the highest recorded scaling strata; the remaining ones captured the next lower one). Finally, for field map *gufm1*, 21 thresholds were defined (spanning the range 400 nT–60 μT, *ca.* 2.2 orders of magnitude), and a total of 92 954 time-series was analysed, of which 61 166 (65.8 per cent) satisfied all significance tests and other quality criteria. The lower percentages of significant results for the two field maps stem from spatially heterogeneous DSI profiles (i.e. some areas display intense preferred scaling, others do not), a topic to be explored in future work.

All of the aforementioned conditions imposed upon subsets had to be met again in the meta-analysis of each primary data set (but with the sign of the power-law slope now required to be positive), and once again for each data set of residuals. In terms of frequency fits, all false-attribution probabilities of the Lomb periodogram peaks remain orders of magnitude below the imposed maximum of 0.10 (which would represent a 5 per cent chance of the true frequency being higher than calculated, and a 5 per cent chance of it being lower). For example, the false attribution probability values for *CALS7K.2*, *SINT2000* and dipole chrons (with superchron included) are 2.81e-47, 3.97e-66 and 1.18e-38, respectively. Confidence in the derived values is further enhanced by the one thousand Monte Carlo bootstrap results per data set (primary and residual data analysed separately), ruling out a chance attribution due to any particular ensemble of points. Secondly, the large sample sizes (due to many thresholds being tested in the subset stage of the analysis) should make the Kuiper test a substantial hurdle, yet almost all data sets pass it even at the 99.9 per cent confidence level (only *SINT2000* and *CALS7K.2* doing slightly less well here).

The argument in favour of significant DSI can alternatively be cast in terms of data residuals. Given that power laws outperform other common probability distributions (such as gamma, Poisson, stretched exponential, normal and lognormal) in these cases, the addition of a superposed log-periodic modulation reduces remaining residuals in the primary data sets on average to 60.5 per cent with respect to the power-law residuals. When the residual, doubled DSI frequency is added, the average drops to 46.9 per cent. For example, the rms-error of the dipole chrons (CNS included) for a power-law fit alone is *ca.* 1.704, whereas the added primary DSI modulation reduces it to 1.108, and the second modulation reduces it further to 0.748.

Finally, in terms of quantification of preferred scales, recall that DSI analysis 'locks in' on the observed log-periodicity based upon *all* intermediate scales (Sornette 1998) as captured in the total spectrum of subsets. Stratae are never assigned casually through identification of local near-horizontal clusters of points, nor using any other kind of eyeballing. The necessary and sufficient conditions for identifying the dominant frequency and associated phase (thereby quantifying stratae) rely on the statistically significant fits, based on a sufficient density of points to rule out aliasing of any higher frequency within relevant range, and a sufficient range of scales to capture one full DSI wavelength or more. Proof of log-periodicity does not call for multiple stratae being observed in a single data set (*SINT2000* and dipole chrons exhibit only one strata), as periodicity in preferred scales is quantified using the full modulation fit, never by measuring the distance between two observed stratae. Nor does proof require a large absolute amplitude of DSI; see the inset in fig. 8 of the companion paper (Jonkers 2007) for amplitude-normalized power-law residuals of *SINT2000* that dis-

play a modulation as clear as *CALS7K.2* does in Fig. 1(C) in this paper.

A separate, but related issue concerns dating errors. One of the key measurements in bootstrapped DSI analysis is time, and the four data sets examined here display wide variability in temporal resolution. For example, the historical field observations that went into *gufm1* are usually accurate to the day or less (Jonkers *et al.* 2002), whereas the error margins on dates of Mesozoic lava depositions that registered dipole reversals can be millennia. However, rather than absolute dates, it is their size relative to the $\log_{10}$ range of studied timescales that determines their potential to degrade the DSI signal. In the latter case of chrons, the range of interest spans $O(10^4$–$10^7)$ yr, making the error margins in Fig. 1(E) vanishingly small. The most troublesome data set in this regard is *SINT2000*, a 'tuned' composite of several different palaeomagnetic ocean cores, prone to age errors due to finite sampling, interpolation approximations, variations in sedimentation rates, and incomplete or inaccurate tie point information. Conservative estimates by Valet *et al.* (2005) and McMillan *et al.* (2004) place the current recovery cut-off at about 20 kyr, that is, well below the preferred timescale derived.

Since bootstrapped DSI analysis does not require equidistantly sampled time-series to work on, a series of tests has been done by adding increasing amounts of white noise to the datings of individual intensity estimates in *SINT2000*, and repeating the entire bootstrap process. The introduced distortions became noticeable at magnitudes of 10–20 kyr, independently validating the findings of McMillan *et al.* (2004). Additional tests with noise-contaminated intensities are described in the companion paper (Jonkers 2007). A different confirmation was obtained by repeating the procedure for subsets of *SINT2000* with temporal windows 2–1 and 1–0 Ma (i.e. 1000 time steps each), based on the assumption that the more recent fluctuations have smaller dating errors on average than the older ones. These tests produced very similar results, differing from the original's DSI parameters by about five percent.

Table 1 also yields the preferred fluctuation size associated with each characteristic duration (with the exception of reversals, for which no such observable is presently available). However, a word of caution is in order here. Although these values are valid within their own empirical context, it would be premature to compare all directly to each other. Not only are those of the dipole intensity data set not expressed in nanoteslas, the two field maps *CALS7K.2* and *gufm1* moreover have different resolution, different damping coefficients, and, as Korte & Constable (2005, figs 6 and 7) have stressed, comparisons of power spectra of main field and secular variation between *gufm1* and *CALS7K.2* consistently show the latter to have less power in all spherical harmonic degrees, in particular when examined at the core–mantle boundary. Consequently, the two archeomagnetic fluctuation scales must be considered substantially too low. Note however, that this does not affect the timescale analysis.

One way to investigate the overall coherence of individual results is through their predicted stratae for ranges beyond those observed, since each observed DSI oscillation can be extrapolated (along its underlying power-law slope) to cover the time spans of other data sets. This is illustrated in Fig. 2, which, for the main observed scaling stratae (vertical bars), plots the closest estimates from primary and first residual modulations for each data set. In Table 2, the observed and predicted stratae derived from secular variation are likewise compared with the closest ones from the palaeomagnetic primary data sets, and in Table 3 with those closest in the palaeomagnetic residual DSI signal. These representations evince once again the difference in quality between secular variation and palaeomagnetic
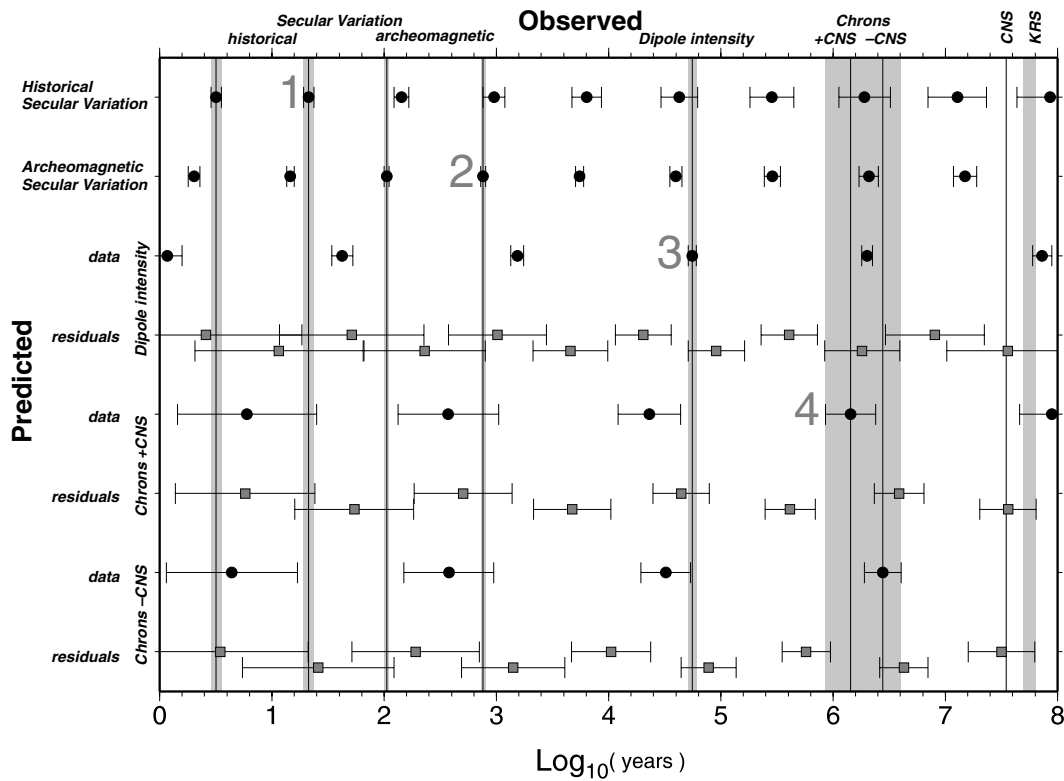
Figure 2. Characteristic geodynamo timescales, based upon observed and extrapolated power-law modulations. At right are marked two superchrons, with current uncertainty regarding the Kiaman Reversed Superchron (KRS) expressed as grey margin. Observed timescales are vertical bars with 2σ error bounds in grey; predicted timescales are symbols with horizontal 2σ error bounds: circles (original data) and squares (residuals after subtracting power law and primary modulation), for secular variation (historical and archeomagnetic), dipole intensity fluctuations, and dipole reversal intervals, with the Cretaceous Normal Superchron (CNS) in- and excluded. Major observed scales are numbered 1–4 (see also Fig. 4).

Table 2. Characteristic geomagnetic timescales in $\log_{10}(\mathrm{yr})$, as observed and predicted with discrete scale invariance, with 2σ error bounds, from *primary* data.

Historical SV	Archeomagnetic SV	Dipole intensity fluctuations	reversal intervals (CNS included)	reversal intervals (CNS excluded)
*0.502 ± 0.046	0.305 ± 0.051		0.778 ± 0.620	0.642 ± 0.582
*1.328 ± 0.045	1.164 ± 0.035	1.627 ± 0.093		
2.153 ± 0.064	*2.023 ± 0.021			
2.979 ± 0.097	*2.882 ± 0.021	3.186 ± 0.058	2.571 ± 0.449	2.575 ± 0.401
3.804 ± 0.130	3.741 ± 0.036			
4.630 ± 0.162	4.599 ± 0.053	*4.744 ± 0.035	4.363 ± 0.277	4.509 ± 0.220
5.455 ± 0.195	5.458 ± 0.070			
6.281 ± 0.228	6.317 ± 0.087	6.303 ± 0.048	*6.156 ± 0.222	*6.442 ± 0.163
7.932 ± 0.293	8.034 ± 0.120	7.862 ± 0.084	7.948 ± 0.287	

Note: SV, secular variation; *, observed; CNS, Cretaceous Normal Superchron.

results, and in particular the poor performance of the data sets of residuals. Error bounds on all bootstrapped DSI results (secular variation and dipole intensity fluctuations) are an order of magnitude smaller than those of chrons and all DSI residual data sets. This not only causes the latter's predictions themselves to be less accurate, but also widens their error margins to the extent that they can no longer discriminate between scales observed far from their own empirical range. It is hoped that future improvements in palaeomagnetic data accuracy will ameliorate this situation.

Nevertheless, Tables 2 and 3 and Fig. 2 suggest that the observed DSI wavelengths can be separated into two main groups: (1) palaeo-magnetic primary data sets and (2) secular variation plus palaeomag-netic residual data sets, with the wavelengths of the first group being approximately double that of the second. This is illustrated with the
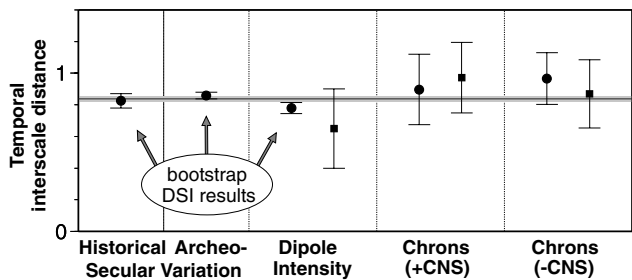
temporal interscale distance (TID), which denotes the log-periodic step size along the time axis (not along the power-law slope) between adjacent scaling stratae. Fig. 3 shows TIDs with their 2σ error margins for all data sets, relative to a Bayesian combined estimate. Note that the TIDs of the primary palaeomagnetic data sets have been divided by two to enable direct comparison. Their similarity (Bayes: 0.84; historical and archeomagnetic secular variation: 0.83 and 0.86; palaeomagnetic primary data: two times 0.78, 0.90 and 0.97; palaeomagnetic residuals: 0.65, 0.97 and 0.87, respectively) spurs the hypothesis that a single DSI signal is expressed directly in the preferred scales of non-dipole secular variation and palaeomag-netic residuals, and at half the frequency in palaeomagnetic primary data sets (dipole fluctuations and reversals). Thus on timescales of $O(10\ \mathrm{Ka})$ and larger, only every second strata of the modulations

Table 3. Characteristic timescales in $\log_{10}(\mathrm{yr})$ of secular variation, compared to the closest preferred timescales derived from palaeomagnetic DSI *residuals*, with 2σ error bounds.

Historical SV	Dipole intensity residuals	Reversal residuals (CNS included)	Reversal residuals (CNS excluded)	Scale step
*0.502 ± 0.046	0.412 ± 0.853	0.761 ± 0.621	0.542 ± 0.783	0.5
*1.328 ± 0.045	1.061 ± 0.749	1.732 ± 0.528	1.411 ± 0.675	1.0
2.153 ± 0.064	2.361 ± 0.644		2.281 ± 0.567	1.5
2.979 ± 0.097	3.010 ± 0.436	2.703 ± 0.436	3.151 ± 0.459	2.0
3.804 ± 0.130	3.660 ± 0.331	3.674 ± 0.343	4.020 ± 0.351	2.5
4.630 ± 0.162	*4.959 ± 0.250	4.645 ± 0.250	4.890 ± 0.244	3.0
5.455 ± 0.195	*5.608 ± 0.250	*5.616 ± 0.222	*5.760 ± 0.215	3.5
6.281 ± 0.228	6.258 ± 0.335	*6.587 ± 0.222	*6.630 ± 0.215	4.0
7.932 ± 0.293	7.557 ± 0.543	7.558 ± 0.250	7.500 ± 0.295	4.5

Note: SV, secular variation; *, observed; CNS, Cretaceous Normal Superchron; last column: see Figs 2 and 4.

Figure 3. Temporal interscale distance (TID) estimates with 2σ confidence intervals, of historical and archeomagnetic secular variation (circles, full-distance) and palaeomagnetic primary (circles, half-distance) and residual (squares, full distance) data sets, compared to a Bayesian estimator ($\sim$0.837) that combines all eight (horizontal bar with 2σ confidence intervals in grey). Chrons are shown separately with Cretaceous Normal Superchron (CNS) in- and excluded. The TIDs of the primary palaeomagnetic data sets have been divided by two to enable direct comparison. The three bootstrap DSI results (on left) are not only far more accurate than the others, but, moreover, yield almost identical values.

observed in secular variation and palaeomagnetic residuals is evident in palaeomagnetic primary data. Those preferred scales that occur in all data sets are, therefore, numbered in Fig. 2 as major scales, whereas the intermediate ones are considered minor scales of the dynamics. Presumably, this contrasting profile stems from analysing different aspects of the complex system, with the major scaling periodicity being more prominently expressed in the global dipole record (intensity fluctuations and reversals), and the intermediary scales being articulated most clearly in local non-dipole field variability, and less strongly in the palaeomagnetic residuals.

Another aspect concerns the error bars of the preferred durations, within the observed range based upon the Monte Carlo results, and multiplied by an appropriate distance factor for other time ranges. This highlights differences in quality and limitations on extrapolation, for example, smaller timescales predicted by chrons primary data and residuals generally are useful only down to the largest preferred scale in archeomagnetic secular variation, and both secular variation data sets perform best for larger timescales than observed. Nevertheless, all error margins are shown in Fig. 2 for completeness and to allow comparison between predictions for the same temporal range by different sources. It also shows the increased effects of noise for residual data with respect to primary data to be worse for dipole intensity fluctuations than for chrons.

More generally, *bottom-up* predictions (that is, those based upon extrapolation to timescales larger than the observed range of a particular data set) tend to be more accurate than *top-down* predic-

tions (those based upon extrapolation to smaller timescales than observed). This cannot be solely attributed to the higher quality of data sets covering the recent past, as even dipole intensity- and chron-based predictors do better above than below their respective observed range. In other words, the geodynamo appears to exhibit a preferred upward direction of coherent scaling. Admittedly, dating and other problems cause all palaeomagnetic results to be inherently less reliable than those of the more recent data sets. However, the 2σ bounds on dipole intensity predictions, for example, are small for chrons and superchrons alike, yet both are almost exactly on target.

Unlike large earthquakes that trigger a cascade of ever-smaller aftershocks, the larger events and durations affecting the geomagnetic field could thus originate in processes at smaller scales. This concurs with several recent multiple-scale dynamo simulations in which clear boundaries between secular variation and larger 'events' no longer exist, and reversals emerge spontaneously out of the long-term evolution of small, locally interacting vortices (Le Mouël *et al.* 1997; Blanter *et al.* 1999; Narteau *et al.* 2000; Narteau & Le Mouël 2005). For experimental evidence of such inverse cascades (vortex coalescence) in freely decaying 2-D turbulence, see Johansen *et al.* (2000b).

Scaling predictions can additionally be extended beyond the timescales of chrons. At the top of Fig. 2 are added the CNS and Kiaman Reversed Superchron (KRS) intervals. The duration of the CNS is well established, so no confidence margins were drawn. By contrast, the duration of the KRS is still debated, so only two recent estimates (315–260 and 311–262 Ma) have been used to draw an upper and lower bound (Eide & Torsvik 1996; Buchan & Chandler 1999). Both CNS and KRS durations are predicted quite well by the observed DSI signatures as observed in shorter-term fluctuations and in palaeomagnetic residuals, suggesting that timescales of $O(10–100$ Ma) could be part of ordinary core dynamics. A related issue (addressed in Section 4) concerns whether or not the CNS should be included in analyses of ordinary chrons and subchrons, or be considered a distinct geomagnetic entity.

Given the similarity of preferred scales in Table 3, the question arises to what extent each of the perceived typical timescales can be associated with known geophysical processes. Regarding the longest intervals, reversals and excursions have already been adequately described and distinguished (e.g. Gubbins 1999); the durations listed in Table 1 simply represent the preferred timescale associated with each of these two types of dipole change. The broad category of secular variation, on the other hand, presents at least four separate timescales of interest. The largest of these is just under $O(1000)$ yr, a duration compatible with archeomagnetic jerks ($\sim$500–1000 yr), with mean azimuthal (east–west) flows ($\sim$1500 yr), and with the estimated convective overturn time ($\geq$500 yr) of the outer core (and

the associated changes in the thermal wind, that is, the non-rigid flows associated with the buoyancy force) (Gallet *et al.* 2003; Dumberry & Bloxham 2006). The next smaller characteristic scale is of $O(100)$ yr, a duration reminiscent of magnetostrophic waves (~300 yr), (Braginsky 1964; Hide 1969; Zatman & Bloxham 1997) and of convective fluctuations in the core about the hydrostatic state (Buffett 1996a).

A prime candidate for attribution of the decadal timescale (of ~20 yr in *gufm1*) are torsional oscillations, a component of the flow predicted by theory (Taylor 1963; Braginsky 1970, 1984, 1993), consisting of azimuthal oscillations of rigid coaxial cylindrical surfaces. These have recently been detected in secular variation (at ~23 yr) (Jault *et al.* 1996; Zatman & Bloxham 1997, 1998; Holme 1998; Hide *et al.* 2000; Pais & Hulot 2000) and correlate well with observed core–mantle exchanges of angular momentum, more specifically, with the associated variations in the length of day (Jackson *et al.* 1993; Jault *et al.* 1996; Zatman & Bloxham 1997, 1998; Holme 1998; Hide *et al.* 2000; Pais & Hulot 2000; Ponsar *et al.* 2003). These studies have moreover been extended to the sub-decadal timescale (of $O(1)$ yr, dubbed 'short-period secular variation,' ~2–6 yr) on which gravitational torques on the inner core may be the most important mechanism of angular momentum exchange (Buffett 1996a, b; Bloxham & Dumberry 2003; Mound & Buffet 2003; Buffett & Mound 2005). Lastly, torsional oscillations have recently been linked to the even shorter timescale of geomagnetic jerks (<1 yr; Bloxham *et al.* 2002; Holme & De Viron 2005), probably the shortest typical geomagnetic fluctuation of internal origin witnessed at the Earth's surface (Courtillot *et al.* 1978; Malin & Hodder 1982; Courtillot & Le Mouël 1984; Mandea *et al.* 2000; Zatman 2001).

A last point concerns the potential interdependence of these geophysical timescales; Holme & De Viron (2005) have argued that geomagnetic jerks and decadal secular variation may have a common origin, and Buffett (1996b) has remarked that oscillations of the inner core (on a subdecadal timescale) can excite torsional oscillations (on a decadal timescale), and vice versa. In addition, geophysical arguments have been put forward to explain preferred geodynamo timescales: Buffett (1996b) has proposed that torsional oscillations may be resonantly amplified at their natural frequency on the decadal timescale, whereas Dumberry & Bloxham (2006) have suggested a resonant excitation of a natural mode of vibration, possibly due to magnetostrophic waves in the core, as an explanation for the preferred millennial timescale of mean zonal flows. These are precisely the kinds of thresholds that could not only give rise to the observed modulations of power-law scaling presented here, but also provide (part of) a geophysical rationale for integrating them into a single scale-free interpretation.

4 CONCLUSION

Four independent geomagnetic data sets (dipole chrons, dipole intensity fluctuations and dipole-detrended archeomagnetic and historical secular variation), spanning very different geodynamo timescales, were found to exhibit similar traits of discrete scale invariance (DSI), that is, a statistically significant modulation superposed on a power-law probability distribution function, relating an observable's fluctuation sizes and durations. The observed scaling signatures are thought to derive from threshold dynamics, due to specific preferred physical scales relevant to the underlying generative process. Using the novel bootstrapped DSI method, data sets were normalized in the temporal domain, allowing predicted scales of one set to be compared directly with observed ones of the oth-

ers, both individually and using a Bayesian estimate of the temporal interscale distance. Despite remaining uncertainties in palaeomagnetic results, the overall coherence found can be interpreted as traits of a single fundamental, primarily bottom-up process driving fluctuations on all analysed geodynamo scales.

Presently, given the assumption of the geodynamo being a complex system that generates fluctuations on many scales, and after applying (bootstrap) DSI analysis to multiple empirical sources that span different parts of its temporal range, a unifying *scaling bridge* may be constructed. This single framework not only covers the entire temporal range of the observed system and reduces the uncertainty margins of individual estimates, but, additionally, predicts other preferred scales not currently described by empirical data.

In total, the various primary and residual data sets provide sixteen observed scaling strata estimates. Provisionally adopting the hypothesis of a single DSI modulation plus a residual doubled frequency, it is possible to assign each of these levels to a specific 'scale step,' arbitrarily numbered in the range from 0.5 to 5, with integers representing stratae of the major oscillation, and minor ones halfway in between. These have been labelled in Fig. 2 (major scales only), tabulated in Table 3 (last column) and plotted in Fig. 4. A simple linear fit (yet another power law) yields intercept –0.456 and slope 1.758, and does a remarkable job of fitting all observed stratae over the entire temporal range. This constitutes the scaling bridge. Note that although the line parameters are arbitrary (since the *x*-values are arbitrary), the linear dependence is not, since the *x*-ratios follow directly from the DSI results in Table 3. To a first approximation, timescales appear log-periodically at increments of ~0.88 $\log_{10}$(yr) per half scale-step along the temporal axis (compare the similar, earlier-stated Bayesian observed estimate of 0.84). In addition, the pervasiveness of DSI in geodynamo time-series is
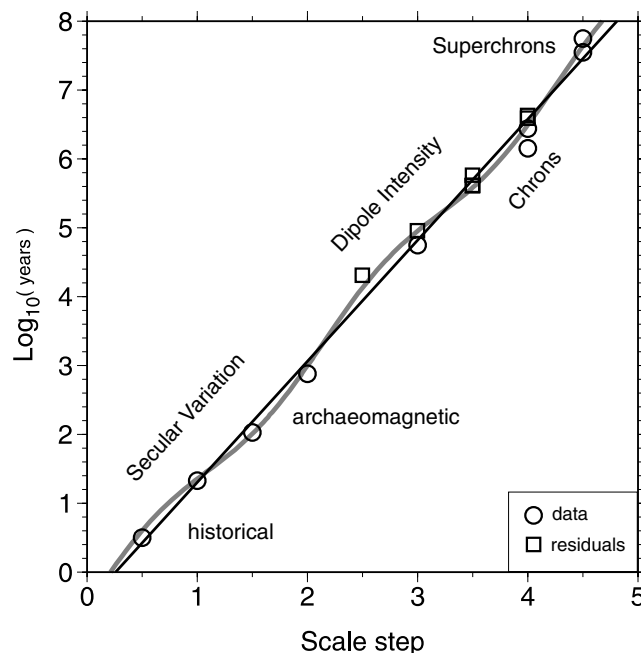
Figure 4. The scaling bridge (see Table 4) connects observed characteristic scales from four independent geomagnetic data sets that jointly span over seven orders of magnitude in time, based upon primary (circles) and residual (squares) power-law modulations. Preferred scales from dipole intensity and chron residuals overlap in scale step 3.5 (see Table 3). Note that the scaling bridge itself also exhibits DSI (grey modulation), which, due to small sample size ($N = 16$), is not statistically significant.

Table 4. Postulated geodynamo timescales from the scaling bridge (power law).

Geodynamo fluctuation type	Scale step	Duration (in yr)	Duration in $\log_{10}$ (yr)
SV (geomagnetic jerk)	0.0	0.35	−0.456
SV (subdecadal)	0.5	2.64	0.422
SV (decadal)	1.0	20.0	1.301
SV (secular)	1.5	151.5	2.180
SV (millennial)	2.0	1147	3.059
Dipole intensity	2.5	8684	3.938
Dipole intensity	3.0	65 745	4.817
Dipole intensity/Chron	3.5	497 739	5.697
Chron	4.0	3 768 253	6.576
Superchron	4.5	28 528 429	7.455
Hectochron	5.0	215 981 032	8.334
Kilochron	5.5	1 635 134 094	9.213

Note: SV, secular variation.

once again stressed by the apparent slight modulation within the scaling bridge itself. Regrettably, the available sixteen points are insufficient to conclude a statistically significant modulation. The durations predicted by the scaling bridge for each strata are listed in Table 4.

On historical timescales, three characteristic scales appear dominant, of $O(1)$, $O(10)$ and $O(100)$ yr, of which only the second one (the one likely associated with torsional oscillations) represents a major scale. Other observed major scales are, respectively, of $O(1$ Ka$)$, $O(10$ Ka$)$ and $O(1$ Ma$)$. On an even shorter timescale than depicted, the bridge can be extended to scale step zero, suggesting a characteristic timescale for geomagnetic jerks of about 128 d (see Table 4). This intriguing possibility will be explored in future work. Table 4 furthermore highlights the continuity of fluctuation durations; no clear demarcation separates historical from archeomagnetic or palaeomagnetic time spans. This is particularly evident in the crossover from *SINT2000* to chron timescales, of which the residual DSI stratae actually coincide in scale step 3.5. In addition, the assignment of characteristic durations to specific steps offers insight concerning the status of superchrons. Apart from the obvious observation that they fit neatly into the general scale-invariant framework, their association with minor scale step 4.5 offers a criterion to in- or exclude them in future analyses of chrons. For example, one could examine only chrons close in duration to the major scale of $O(1$ Ma$)$, or alternatively, widen the spectrum to include the nearest two minor scales, or an even broader set. However, the current practice of considering subchrons and chrons as more similar to one another than to superchrons cannot be supported from a scale-invariant perspective; they are merely three successive scale steps in a longer progression. The question as to whether the geodynamo exhibits even larger preferred timescales than a superchron [notably, a hectochron of $O(10^8$ yr$)$, and a kilochron of $O(10^9$ yr$)$] will have to await longer, high-quality palaeomagnetic records than are presently available. The study of DSI in sufficiently long numerical and laboratory dynamo simulations provide two alternative approaches that seem more feasible in the immediate future.

The scaling bridge constitutes a coherent interpretation of internal geomagnetic fluctuations of all sizes. Threshold dynamics can be thought to separate preferred durations and associated magnitudes of change, with a great many localized short-period fluctuations forming bottom-up cascades (Braginsky & Meytlis 1990; Frick & Roberts 1995; Johansen *et al.* 2000b; Biferale 2003), producing emergent features at each higher level of resolution, and with contingent change dependent on external constraints and the system's own long-term history (Narteau *et al.* 2000; Jonkers 2003). The geo-

dynamo can therewith be considered a single scale-free system with extremely long-term memory, pervaded by DSI-modulated power laws that jointly span over seven orders of magnitude in time, possibly more. Specific events such as geomagnetic jerks, core spots, archeomagnetic jerks, mean zonal flows, dipole intensity fluctuations, reversals and even superchrons can thereby be interpreted as internally controlled units of secular variation associated with a particular threshold, preferred interval and physical size (Sarson & Jones 1999; Coe *et al.* 2000; Love 2000; Hulot & Gallet 2003; Narteau & Le Mouël 2005). Together, these characteristic scales provide a quantified profile with which to constrain the relevant physics.

ACKNOWLEDGMENTS

REFERENCES

Biferale, L., 2003. Shell models of energy cascade in turbulence, *Ann. Rev. Fluid. Mech.,* **35,** 441–468.

Blanter, E.M., Narteau, C., Shirnman, M.G. & Le Mouël, J.-L., 1999. Up and down cascade in a dynamo model: spontaneous symmetry breaking, *Phys. Rev. E,* **59**(5), 5112–5123.

Bloxham, J. & Dumberry, M., 2003. Towards a physical understanding of the short-period secular variation, *EGU Geophys. Res. Abstr.,* **5,** 05996.

Bloxham, J., Zatman, S. & Dumberry, M., 2002. The origin of magnetic jerks, *Nature,* **420,** 65–68.

Braginsky, S.I., 1964. Magnetohydrodynamics of the Earth's core, *Geomag. Aeron.,* **4,** 698–712.

Braginsky, S.I., 1970. Torsional magnetohydrodynamics vibrations in the Earth's core and variations in day length, *Geomagn. Aeron.,* **10,** 3–12 (Engl. transl. 1–8).

Braginsky, S.I., 1984. Short-period geomagnetic secular variation, *Geophys. Astrophys. Fluid Dyn.,* **30,** 1–78.

Braginsky, S.I., 1993. MAC oscillations of the hidden ocean of the core, *J. Geomagn. Geoelectr.,* **45,** 1517–1538.

Braginsky, S.I. & Meytlis, V.P., 1990. Local turbulence in the Earth's core, *Geophys. Astrophys. Fluid Dyn.,* **55,** 71–87.

Buchan, K.L. & Chandler, F.W., 1999. Paleomagnetism of the distal member of the New Glasgow Formation, Nova Scotia, Canada: new constraints on

magnetic polarity stratigraphy near the base of the Kiaman superchron, *J. Geol.,* **107,** 271–286.

Buffett, B.A., 1996a. Gravitational oscillations in the length of day, *Geophys. Res. Lett.,* **23**(17), 2279–2282.

Buffett, B.A., 1996b. A mechanism for decade fluctuations in the length of day, *Geophys. Res. Lett.,* **23**(25), 3803–3806.

Buffett, B.A. & Mound, J.E., 2005. A Green's function for the excitation of torsional oscillations in the Earth's core, *J. Geophys. Res.,* **110,** B08104. doi:10.1029/2004JB003495

Coe, R.S., Hongre, L. & Glatzmaier, G., 2000. An examination of simulated geomagnetic reversals from a palaeomagnetic perspective, *Phil. Trans. R. Soc. Lond. A,* **358,** 1141–1170.

Constable, C.G., Johnson, C.L. & Lund, S.P., 2000. Global geomagnetic field models for the past 3000 yr: transient or permanent flux lobes? *Phil. Trans. R. Soc. Lond. A,* **358,** 991–1008.

Courtillot, V., Ducruix, J. & Le Mouël, J.-L., 1978. Sur une accélération récente de la variation séculaire du champ magnétique terrestre, *C. R. Acad. Sci. Paris D,* **287,** 1095–1098.

Courtillot, V. & Le Mouël, J.-L., 1984. Geomagnetic secular variation impulses, *Nature,* **311,** 709–716.

Dormy, E., Valet, J.-P. & Courtillot, V., 2000. Numerical models of the geodynamo and observational constraints, *Geochem. Geophys. Geosys.,* **1,** 2000GC000062.

Dumberry, M. & Bloxham, J. 2006. Azimuthal flows in the Earth's core and changes in LOD at millennial timescales, *Geophys. J. Int.,* **165,** 32–46.

Eide, E.A. & Torsvik, T.H., 1996. Paleozoic supercontinental assembly, mantle flushing, and genesis of the Kiaman Superchron, *Earth Planet. Sci. Lett.,* **144,** 389–402.

Frick, P. & Roberts, P.H., 1995. Cascade and dynamo action in a shell model of magnetohydrodynamic turbulence, *Phys. Rev. E.,* **57,** 4155–4164.

Gallet, Y., Genevey, A. & Courtillot, V., 2003. On the possible occurrence of archaeomagnetic jerks in the geomagnetic field over the past three millenia, *Earth Planet. Sci. Lett.,* **214,** 237–242.

Glatzmaier, G.A., Coe, R.S., Hongre, L. & Roberts, P.H., 1999. The role of the Earth's mantle in controlling the frequency of geomagnetic reversals, *Nature,* **401,** 885–890.

Gradstein, F.M. & Ogg, J., 1996. A Phanerozoic timescale, *Episodes,* **19**(1–2), 3–5.

Gubbins, D., 1999. The distinction between geomagnetic excursions and reversals, *Geophys. J. Int,* **137,** F1–F3.

Hide, R., Boggs, D.H. & Dickey, J.O., 2000. Angular momentum fluctuations with the Earth's liquid core and torsional oscillations of the core-mantle system, *Geophys. J. Int.,* **143,** 777–786.

Hollerbach, R., 2003. The range of timescales on which the geodynamo operates, in *Earth's Core: Dynamics, Structure, Rotation,* pp. 181–192, eds Dehant, V., Creager, K.C. & Karato, S., Zatman, S., AGU Geodynamics Series 31, AGU, Washington DC.

Holme, R., 1998. Electromagnetic core-mantle coupling-I. Explaining changes in the length of day, *Geophys. J. Int.,* **132,** 167–180.

Holme, R. & De Viron, O. 2005. Geomagnetic jerks and a high-resolution LOD profile for core studies, *Geophys. J. Int.,* **160,** 435–439

Holme, R. & Olsen, N., 2006. Core-surface flow modelling from high resolution secular variation, *Geophys. J. Int.,* **166,** 518–528.

Hongre, L., Hulot, G. & Khokhlov, A., 1998. An analysis of the geomagnetic field over the past 2000 yr, *Phys. Earth Planet. Int.,* **106,** 311–335.

Hulot, G. & Gallet, Y., 2003. Do superchrons occur without any palaeomagnetic warning? *Earth Planet. Sci. Let.,* **210,** 191–201.

Jackson, A., Bloxham, J. & Gubbins, D., 1993. Time-dependent flow at the core surface and conservation of angular momentum in the coupled core-mantle system, in *Dynamics of the Earth's Deep Interior and Earth Rotation,* Vol. 72, pp. 97–107, eds Le Mouël, J.-L., Smylie, D.E. & Herring, T.A., AGU Geophysical Monograph, Washington, DC.

Jackson, A., Jonkers, A.R.T. & Walker, M., 2000. Four centuries of geomagnetic secular variation from historical records, *Phil. Trans. R. Soc. Lond. A,* **358,** 956–990.

Jault, D., Gire, C. & Le Mouël, J.-L., 1988. Westward drift, core motions and exchanges of angular momentum between core and mantle, *Nature,* **333,** 353–356.

Jault, D., Hulot, G. & Le Mouël, J.-L., 1996. Mechanical core-mantle coupling and dynamo modelling, *Phys. Earth Planet. Int.,* **98,** 187–191.

Johansen, A., Saleur, H. & Sornette, D., 2000a. New evidence of earthquake precursor phenomena in the 17 January 1995Kobe earthquake, Japan, *Eur. Phys. J.,* **B15,** 551–555.

Johansen, A. & Sornette, D., 1998. Evidence of discrete scale invariance in DLA and time-to-failure by canonical averaging, *Int. J. Mod. Phys.,* **C9**(3), 433–447.

Johansen, A., Sornette, D. & Espe Hansen, A., 2000b. Punctuated vortex coalescence and discrete scale invariance in two-dimensional turbulence, *Physica D,* **138,** 302–315.

Jonkers, A.R.T., 2003. Long-range dependence in the Cenozoic reversal record, *Phys. Earth Planet. Int.,* **135,** 253–266.

Jonkers, A.R.T., 2007. Bootstrapped discrete scale invariance analysis of geomagnetic dipole intensity, *Geophys. J. Int.,* **169**(2), 646–658.

Jonkers, A.R.T., A. Jackson & A. Murray, 2002. Four centuries of geomagnetic data from historical records, *Rev. Geophys.,* **41**(2), 1006.

Korte, M. & Constable, C.G., 2003. Continuous global geomagnetic field models for the past 3000 yr, *Phys. Earth Planet. Int.,* **140,** 73–89.

Korte, M. & Constable, C.G., 2005. Continuous geomagnetic field models for the past 7 millennia II: CALS7K,. *Geochem. Geophys. Geosyst.,* **6,** Q02H16, doi:10/2004GC000801.

Korte, M., Genevey, A., Constable, C.G., Frank, U. & Schnepp, E., 2005. Continuous geomagnetic field models for the past 7 millennia I: a new global data compilation, *Geochem. Geophys. Geosyst.,* **6,** Q02H15, doi:10.1029/2004GC000800.

Langereis, C.G., Dekkers, M.J., Lange, G.J. de, Paterne, M. & Santvoort, P.J.M. van, 1997. Magnetostratigraphy and astronomical calibration of the last 1.1 Myr from an eastern Mediterranean piston core and dating of short events in the Brunhes, *Geophys. J. Int.,* **129,** 75–94.

Le Mouël, J.-L., Allègre, C.J. & Narteau, C., 1997. Multiple scale dynamo, *Proc. Nat. Acad. Sci.,* **94,** 5510–5514.

Love, J.J., 2000. Paleomagnetic secular variation as a function of intensity, *Phil. Trans. R. Soc. Lond. A,* **358,** 1191–1223.

Lu, E.T. & Hamilton, R.J., 1991. Avalanches and the distribution of solar flares, *Astroph. J.,* **380,** L89–L92.

Lu, E.T., Hamilton, R.J., McTiernan, J.M. & Bromund, K.R., 1993. Solar flares and avalanches in driven dissipative systems, *Astroph. J.,* **412,** 841–852.

Malin, S.R.C. & Hodder, B.M., 1982. Was the 1970 geomagnetic jerk of internal or external origin? *Nature,* **296,** 726–728.

Mandea, M., Bellanger, E. & Le Mouël, J.-L., 2000. A geomagnetic jerk for the end of the 20th century? *Earth Planet. Sci. Lett.,* **183,** 369–373.

McMillan, D.G., Constable, C.G. & Parker, R.L., 2004. Assessing the dipolar signal in stacked paleointensity records using a statistical error model and geodynamo simulations, *Phys. Earth Planet. Int.,* **145,** 37–54.

Mound, J.E. & Buffett, B.A., 2003. Interannual oscillations in length of day: implications for the structure of the mantle and core, *J. geophys. Res.,* **108**(B7), 2334, doi:10.1029/2002JB002054.

Narteau, C., Blanter, E., Le Mouël, J.-L., Shirnman, M. & Allègre, C.J., 2000. Reversal sequence in a multiple scale dynamo mechanism, *Phys. Earth Planet. Int.,* **120,** 271–287.

Narteau, C. & Le Mouël, J.-L., 2005. Transient evolution regimes in a multiscale dynamo model: time scales of the reversal mechanism, *J. geophys. Res.,* **110,** B01104, doi:10.1029/2004JB002983.

Novikov, E.A., 1990. The effect of intermittency on statistical characteristics of turbulence and scale similarity of breakdown coefficients, *Phys. Fluids A,* **2,** 814–820.

Pais, A. & Hulot, G., 2000. Length of day variations, torsional oscillations, and inner core super-rotation: evidence from recovered core surface zonal flows, *Phys. Earth Planet. Int.,* **118,** 291–316.

Pelletier, J.D., 1999. Paleointensity variations of Earth's magnetic field and their relationship with polarity reversals, *Phys. Earth Planet. Int.,* **110,** 115–128.

Pelletier, J.D., 2002. Natural variability of atmospheric temperatures and geomagnetic intensity over a wide range of time scales, *Proc. Nat. Acad. Sci.,* **99**(Suppl. 1), 2546–2553.

Ponsar, S., Dehant, V., Holme, R., Jault, D., Pais, A. & van Hoolst, T., 2003. The core and fluctuations in the Earth's rotation, in *Earth's Core: Dynamics, Structure, Rotation,* Vol. 31, pp. 251–261, eds Dehant, V., Creager, K.C., Karato, S.-I. & Zatman, S., Geodyn.Ser., AGU Geophysical Monographs, Washington, DC.

Roberts, P.H. & Glatzmaier, G.A., 2000. Geodynamo theory and simulations, *Rev. Mod. Phys.,* **72,** 1081–1123.

de Santis, A., Barraclough, D.R. & Tozzi, R., 2003. Spatial and temporal spectra of the geomagnetic field and their scaling properties, *Phys. Earth Planet. Int.,* **135,** 125–134.

Sarson, G.R. & Jones, C.A., 1999. A convection driven geodynamo reversal model, *Phys. Earth Planet. Int.,* **111,** 3–20.

Sornette, D., 1998. Discrete-scale invariance and complex dimensions, *Phys. Rep.,* **297,** 239–270.

Sornette, D., 2004. *Critical Phenomena in Natural Sciences: Chaos, Fractals, Self-organization and Disorder: Concepts and Tools,* 2nd edn, Springer, Heidelberg.

Sornette, D., Johansen, A., Arneodo, A., Muzy, J.F. & Saleur, H., 1996. Complex fractal dimensions describe the hierarchical structure of diffusion-limited aggregate clusters, *Phys. Rev. Lett.,* **76,** 251–254.

Stacey, F.D. & Anderson, O.L., 2001. Electrical and thermal conductivities of Fe-Si-Ni alloys under core conditions, *Phys. Earth Planet. Int.,* **124,** 153–162.

Taylor, J.B., 1963. The magneto-hydrodynamics of a rotating fluid and the Earth's dynamo problem, *Proc. R. Soc. Lond. A,* **274,** 274–283.

Valet, J.-P., Meynadier, L. & Guyodo, Y., 2005. Geomagnetic dipole strength and reversal rate over the past two million years, *Nature,* **435,** 802–805.

West, B.J. & Shlesinger, M.F., 1989. On the ubiquity of *1/f* noise, *Int. J. Mod. Phys. B,* **3**(6), 795–819.

Zatman, S., 2001. Phase relations for high frequency core-mantle coupling and the Earth's angular momentum budget, *Phys. Earth Planet.Int.,* **128,** 163–178.

Zatman, S. & Bloxham, J., 1997. Torsional oscillations and the magnetic fields within the Earth's core, *Nature,* **388,** 760–763.

Zatman, S. & Bloxham, J., 1998. A one-dimensional map of *Bs* from torsional oscillations of the Earth's core, in *The Core-Mantle Boundary Region,* Vol. 28, pp.183–196, eds Gurnis, M., Wysession, M.E., Knittle, E. & Buffett, B.A., Geodyn.Ser. AGU Geophys. Monograph, Washington, DC.

Zhang, K. & Gubbins, D., 2000. Scale disparities and magnetohydrodynamics in the Earth's core, *Phil. Trans. R. Soc. Lond. A,* **358,** 899–920.

Zhou, W.-X. & Sornette, D., 2002. Evidence of intermittent cascades from discrete hierarchical dissipation in turbulence, *Physica D,* **165,** 94–125.

SUPPLEMENTARY MATERIAL

The following supplementary material is available for this article:

Appendix S1. Contains Tables S1 to S3 and Figs S1 to S4.

This material is available as part of the online article from: http://www.blackwell-synergy.com/doi/abs/10.1111/j.1365-246X.2007.03551.x (this link will take you to the article abstract).

Please note: Blackwell Publishing are not responsible for the content or functionality of any supplementary materials supplied by the authors. Any queries (other than missing material) should be directed to the corresponding author for the article.